(Received 1 November 2025, Accepted 14 December 2025, Scheduled 24 December 2025)

A Compact CPW-Fed Super-Wideband Antenna on FR4 for 5G, 6G, and Wireless Applications

Manish Kumar[1], Sandeep K. Singh[1,*], Madhukar Deshmukh[1], and Siti N. F. Yusuf[2]

[1] *Department of EECE, SUSET, Sharda University, Greater Noida 201306, India*
[2] *Centre for Ionics University of Malaya, Department of Physics*
Faculty of Science, University of Malaya, Kuala Lumpur 50603, Malaysia

ABSTRACT: This work presents a compact coplanar waveguide (CPW) fed super wideband (SWB) antenna realized on a low-cost FR4 substrate $\varepsilon_r = 4.4$, thickness $= 1.6$ mm). The $20 \times 20\,\text{mm}^2$ radiator integrates a multi-slotted patch within a hexagonal ground plane aperture and a carefully optimized tuning stub that excites and merges multiple resonances into a continuous broadband response. The antenna achieves a measured $|S_{11}| \leq -10$ dB impedance bandwidth (IBW) from 2 to 34 GHz (177.7%), encompassing sub-6 GHz 5G, WLAN/WiMAX, and millimeter wave (Ku/Ka) allocations. Radiation measurements reveal quasi-omnidirectional patterns with a peak gain of 6.60 dB and maximum radiation efficiency of 82.68%. Time-domain analysis demonstrates an almost constant group delay (approximately 0.1 to 0.5 ns, mean 0.19 ns) with a single localized deviation near 24.4 GHz, confirming low dispersion and excellent phase linearity, which are desirable for IR-UWB and high data rate communication systems. Parametric optimization and equivalent RLC circuit modeling validate the broadband mechanism, while simulation studies performed using CST Microwave Studio exhibit excellent agreement with experimental results. The proposed design therefore offers a cost-effective, compact, and high-performance antenna solution suitable for 5G/6G front ends, radar imaging, and broadband sensing applications.

1. INTRODUCTION

The relentless evolution of wireless technology, driven by applications such as Fifth-Generation/Sixth-Generation (5G/6G) mobile networks, the Internet of Things (IoT), and high-definition streaming, necessitates antennas with ultra-large bandwidth, high data rates, compact form factors, and low power consumption [1–4]. While ultra-wideband (UWB) antennas (with a bandwidth ratio of $\sim 3.4:1$) offer significant bandwidth, their limitations in radiation efficiency, frequency coverage, and pattern stability have prompted the development of SWB antennas. SWB antennas, typically defined by a bandwidth ratio exceeding $10:1$, are capable of supporting a vast spectrum from sub-6-GHz to millimeter-wave (mmWave) bands, including UWB, Wireless Local Area Network (WLAN), Worldwide Interoperability for Microwave Access (WiMAX), C, X, Ku, Ka, and 5G NR services, making them indispensable for next-generation communication and sensing systems [5–7].

Considerable research effort has been devoted to compact CPW-fed and microstrip antennas that realize wide or ultra-wide impedance bandwidths and, in many cases, circular polarization, Multiple-Input Multiple-Output (MIMO) capability, or imaging performance enhancements [5–12]. Foundational transmission-line and strip/slot modeling provides the theoretical basis for these structures and guides equivalent-circuit interpretations of their broadband behaviour [13]. Building on this foundation, a wide variety of printed UWB and SWB antennas employing modified monopoles, fractal geometries, and diversity techniques have been reported for communication and sensing applications, including breast and head imaging, circularly polarized operation, and multi-band or multi-standard coverage [14–21]. Broadband slot and patch configurations such as U-slots and E-shapes further demonstrate how carefully shaped resonant apertures can expand impedance bandwidth while preserving radiation characteristics [22, 23]. In parallel, substrate studies emphasize that dielectric choice strongly influences bandwidth, efficiency, and gain, particularly when transitioning from low-loss materials to low-cost FR4 [24].

To address these challenges, numerous UWB/SWB slot and CPW-fed antennas have been proposed on both high-performance and inexpensive substrates, exploiting open-slot configurations, metamaterial loading, and other miniaturization strategies to enhance bandwidth and gain [25, 26]. More recently, hexagonal and fractal SWB MIMO antennas have been introduced to achieve large ratio bandwidths with improved isolation and pattern diversity [27]. Classical antenna-theory treatments continue to provide design guidelines and closed-form estimates for resonant dimensions and input impedance, which are essential when integrating multiple resonant features into a compact radiator [28]. In addition, several compact circularly polarized and UWB monopole/slot antennas have been developed to support Global System for Mobile Communications (GSM), WiMAX, Industrial, Scientific, and Medical (ISM) band, WLAN, and emerging broadband links within a single platform [29, 30]. A compact offset elliptical-ring SWB patch antenna for 5G applications

* Corresponding author: Sandeep Kumar Singh (sandeepsingh.ec@dr.sharda.ac.in).

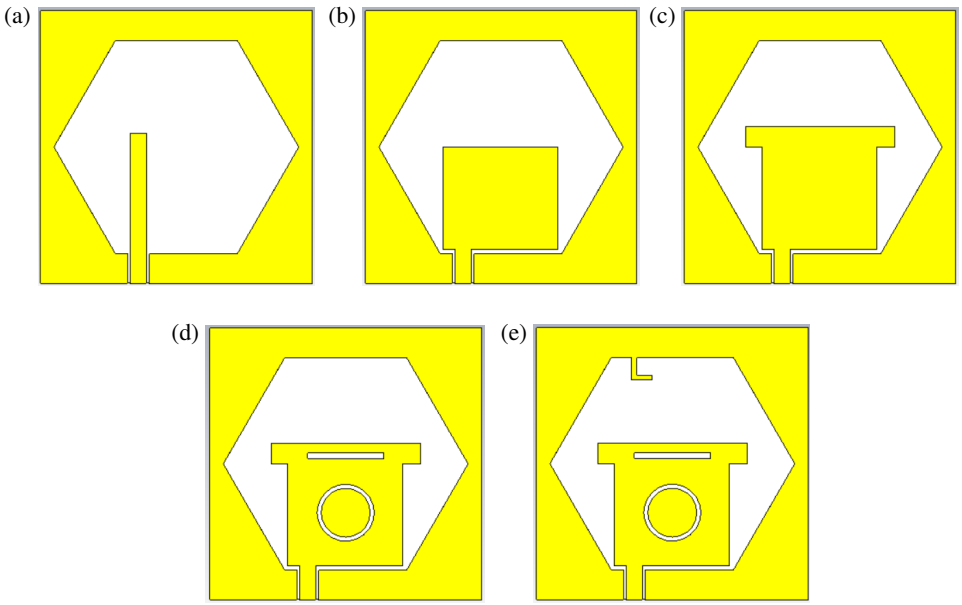

FIGURE 1. Different phases of proposed antenna evolution.

further illustrates the trend toward extreme bandwidth and miniaturization in printed antennas [31].

This analysis reveals a clear research gap: there is a lack of truly compact, low-cost antenna designs that can deliver both extreme bandwidth ($> 175\%$) and high gain (> 6 dB) on a standard, lossy FR4 substrate. Most existing work compromises on one of these critical metrics: size, cost, bandwidth, or gain.

The novelty and contribution of this work address this gap by proposing a compact $20 \times 20\,\text{mm}^2$ CPW-fed SWB antenna on standard glass-reinforced epoxy laminate FR4, where a hexagonal ground aperture, a multi-slotted patch, and a tuning stub are integrated to control surface currents and merge multiple resonances into a single super-wide band. The main contributions are:

1. **Exceptional Performance on Low-Cost Material:** The antenna achieves a measured 2–34 GHz bandwidth (177.7%), Ratio Bandwidth (RBW) of $17:1$, Bandwidth Dimension Ratio (BDR) of $9996\%/\lambda^2$, and 6.60 dB peak gain. As shown in Table 3, this combination of bandwidth, size, and gain is among the strongest reported for FR4-based UWB/SWB antennas.

2. **Comprehensive Design Insight:** Parametric studies, surface-current analysis, and a lumped RLC equivalent-circuit model explain how the hexagonal aperture, patch slots, and stub jointly produce the SWB response. Phase and group-delay analysis further support the design methodology, providing clear guidelines for similar compact CPW-fed SWB antennas.

Compared with prior FR4-based CPW-fed UWB/SWB antennas [3, 7–12, 16, 17, 19, 20, 27, 29, 30], which typically rely on isolated radiator or ground modifications and often compromise size, gain, or RBW, the proposed design uniquely combines a compact $20 \times 20\,\text{mm}^2$ footprint with a measured 2–34 GHz SWB response (177.7%, RBW $17:1$) and 6.60 dB gain using a single-layer CPW feed. As summarized in Table 3, among FR4-based designs, only a few antennas exhibit comparable or higher RBW ([3, 27, 29, 31]), yet they either occupy significantly larger areas ($30 \times 30\,\text{mm}^2$ or $40 \times 30\,\text{mm}^2$ in [3] and [31], $23.5 \times 35\,\text{mm}^2$ in [27], $68 \times 33\,\text{mm}^2$ in [29]) or suffer from notably lower peak gains (4.45 dB in [27] and 1.85 dB in [29]) over their bands, whereas the proposed antenna maintains both wide bandwidth and relatively high gain in a much smaller footprint. This performance is enabled by a systematically engineered multi-resonant structure combining a hexagonal aperture, a multi-slotted patch, and a ground stub rather than geometry-only tuning. Owing to this wide coverage, the antenna supports sub-6 GHz 5G NR, Long-Term Evolution (LTE), WiMAX, WLAN, C/X/Ku radar and imaging bands, and the 24–30 GHz region relevant to millimeter-wave 5G and emerging 6G links. As such, the proposed FR4-based SWB antenna provides a high-performance, low-cost solution suitable for 5G/6G front ends, broadband wireless systems, and microwave sensing or imaging platforms.

The article comprises three sections. Section 2 addresses antenna design and evolution. Section 3 presents the measured results and analysis of the proposed antenna, and Section 4 concludes the proposed work.

2. ANTENNA DESIGN AND EVOLUTION

Figure 1 shows the evolution of the antenna. The main radiating element of the antenna is rectangular, positioned inside a hexagonal slot engraved into the ground plane. The hexagonal cut ground loaded with a stub and rectangular slit on the patch will generate a super wide bandwidth. Circular and rectangu-

TABLE 1. Dimension of the proposed antenna.

Dimension	Unit (mm)	Dimension	Unit (mm)	Dimension	Unit (mm)
a	20	f	7.50	k	1.59
b	20	g	1.50	l	1.50
c	9	h	5.60	m	3.60
d	6.50	i	1.30	n	4.20
e	11	j	1.20	o	0.40

lar slots on the patch improve impedance matching and provide direction for currents generated in the patch and ground.

2.1. Antenna Geometry Analysis

The structural modeling of the antenna is the most significant aspect of designing the specific antenna. Antenna structure models are developed using various materials and geometries. The geometries are utilized to improve the antenna characteristics, specifically the return loss ($|S_{11}|$), bandwidth, radiation pattern, and gain. Here, it provides mathematical modeling to evaluate the antenna dimensions and the optimization methods used to enhance its performance. Selecting an appropriate antenna size makes it suitable for different wireless applications. Figure 2 depicts the proposed antenna geometry. An antenna measuring $20 \times 20 \times 1.6\,\text{mm}^3$ is fabricated on a FR4 substrate after modeling with Computer Simulation Technology-Microwave Studio (CST-MW) studio software. Table 1 shows the overall dimensions.

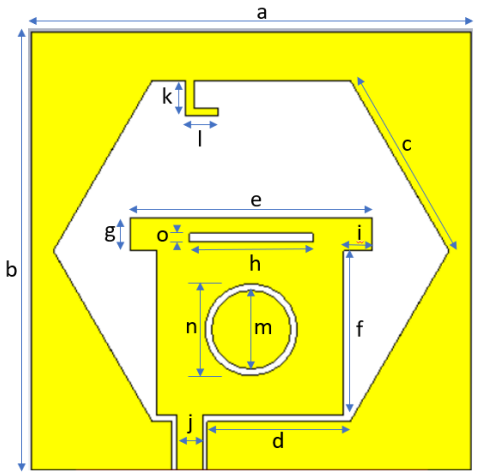

FIGURE 2. Design layout of the proposed antenna.

The patch's length L and width W, corresponding to the physical length and width of the rectangular radiating patch shown in Figure 2, primarily determine its fundamental resonant frequency f_r, radiation pattern, and input impedance. In this work, the initial values of L and W are obtained using the conventional microstrip patch design relations for the dominant TM_{10} mode on a grounded dielectric substrate, which link the effective dielectric constant, guided wavelength, and desired f_r to the physical dimensions of the patch. These standard expressions are well documented in [28] for full details. Using the target resonance and substrate parameters ($\varepsilon_r = 4.4$, $h = 1.6\,\text{mm}$), the initial patch dimensions are first calculated from [28] and then slightly tuned in CST to accommodate the hexagonal aperture and slot-loaded configuration, while preserving good impedance matching over the intended band.

2.2. Resonance Mechanism of Slots and Stubs

The standard microstrip patch relations summarized in [28] provide a starting point for sizing the primary radiating structure. However, the SWB performance is achieved by introducing multiple closely spaced resonances through strategic modifications. The resonant frequencies of these added features can be approximated to understand their contribution to the overall bandwidth.

The introduction of a slot in the patch or ground plane creates an additional resonant path. The fundamental resonant frequency of a narrow rectangular slot (Equation (1)) of length L_{slot} can be approximated by considering it as a half-wavelength resonator [28]:

$$f_{r_{slot}} \approx \frac{c}{2L_{slot}\sqrt{\varepsilon_{eff\_slot}}} \tag{1}$$

where ε_{eff_slot} is the effective dielectric constant for the slot, which is influenced by the substrate and the surrounding geometry.

Similarly, the stub loaded in the ground plane acts as a parasitic element. Its resonant frequency (Equation (2)), when modeled as a short-length transmission line, is given by:

$$f_{r_{stub}} \approx \frac{c}{4L_{stub}\sqrt{\varepsilon_{eff\_stub}}} \tag{2}$$

where L_{stub} is the physical length of the stub. The factor of 4 arises from the assumption that the stub is terminated in a high-impedance (open) condition at its end, creating a quarter-wave resonance.

In the proposed design, the circular slot can be approximated by an equivalent rectangular slot or a loop with an effective length $L_{circular} = \pi r$, where r is its radius. The synergistic interaction of these multiple resonators: the main patch (f_{r_patch}), the rectangular slit (f_{r_slit}), the circular slot (f_{r_circ}), and the ground stub (f_{r_stub}), creates multiple resonances. These resonant paths collectively enable a wideband impedance matching.

2.3. Parametric Study

The proposed SWB antenna's design and optimization procedures are shown in Figures 1–3. Using the trial-and-error

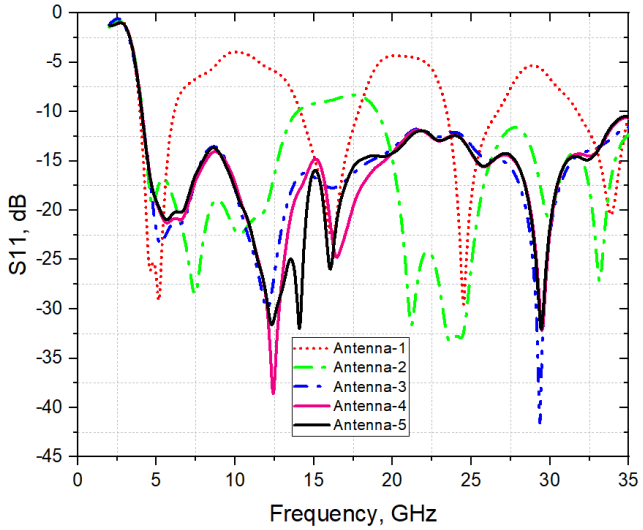

FIGURE 3. Simulation performance of $|S_{11}|$ at different design stages.

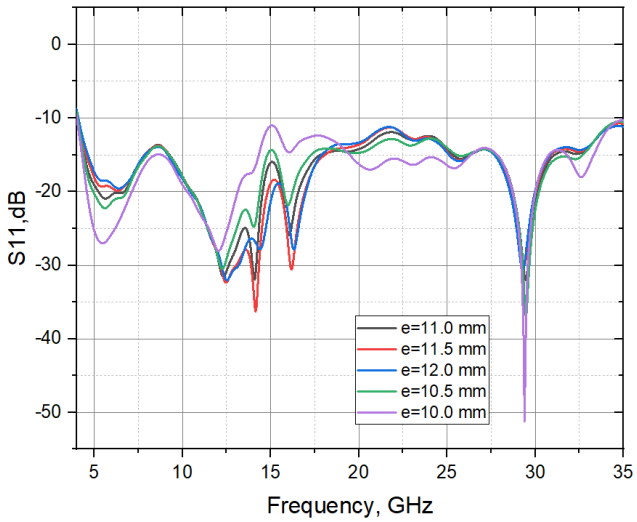

FIGURE 4. Impact of rectangular slit width on $|S_{11}|$.

method, the SWB frequency range and $|S_{11}|$ performance were tuned by adjusting the external dimensions and incorporating slits/slots in the patch and ground plane. Figure 3 illustrates how these geometric modifications influence the input reflection characteristics of the CPW-fed antenna across the 4–35 GHz range using the same FR4 substrate and dimensions.

The evolutionary design of the proposed antenna, detailed in Figures 1(a)–(e) and its corresponding simulated $|S_{11}|$ performance in Figure 3, follows a systematic progression toward achieving SWB operation. The initial design (Antenna 1), comprising a CPW-fed rectangular patch inset within a hexagonal ground aperture, functioned as a multi-resonator but exhibited poor impedance matching, yielding four discrete narrow bands between 4–35 GHz. Refinement of the patch geometry (Antenna 2) significantly improved impedance matching, combining these resonances into two broader bands centered near 9 GHz and 26.95 GHz. Introducing a rectangular slit at the top of the patch (Antenna 3) extended the current path, excited an additional lower-frequency resonance, and effectively bridged the existing bands. Further improvement was achieved by incorporating circular and rectangular slots into the patch (Antenna 4), which perturbed current distributions and introduced multiple closely spaced resonances that strengthened in-band matching. The final design (Antenna 5) integrated a tuning stub into the ground plane, acting as a quarter-wavelength parasitic resonator to generate an additional mode and unify the resonant structure. This resulted in a continuous and well-matched SWB impedance response with a simulated bandwidth of 159% (4–35 GHz).

To comprehend the proposed antenna's operation, different design parameters and configurations have been investigated. Figures 4, 5, and 6 compare the $|S_{11}|$ responses for variations in key geometric parameters: Figure 4 shows the effect of changing the rectangular slit width 'e', Figure 5 the slit length 'g', and Figure 6 the stub width 'l'. Adding rectangular and circular ring slots increases the reflection-coefficient depth to -38.4 dB and -25 dB at 12.5 GHz and 16.5 GHz, respectively. The additional rectangular strip introduces new radiating edges, enhancing surface-current distribution and modifying the antenna impedance. In Figure 6, increasing the stub width (and its effective electrical length) lowers the corresponding resonant frequency, consistent with the relation $f_r \propto 1/L_{\mathrm{b}}$. This behavior demonstrates how the stub and slot geometries contribute to smooth broadband impedance matching.

The surface current density at 6 GHz, 12.5 GHz, 14 GHz, 16 GHz, and 29.5 GHz is displayed in Figure 7, and these current distribution plots summarize the design strategy that was followed while evolving from Antenna 1 to Antenna 5. At 6 GHz (Figure 7(a)), strong currents are concentrated along the inner boundary of the hexagonal ground aperture and the CPW feed transition, while relatively weak currents appear in the central region of the patch. This observation indicates that the low-frequency resonance is mainly governed by the effective loop around the hexagonal cut and motivates preserving and slightly enlarging this current path rather than increasing the patch size. At 12.5 GHz and 14 GHz (Figure 7(b) and Figure 7(c)), the current density becomes strongly localized around the rectangular slit and circular slot in the patch, confirming that these features introduce additional half-wavelength resonant paths that support mid-band resonances and improve impedance matching, consistent with the evolution from Antennas 2 to 4 and the $|S_{11}|$ trends in Figures 3, 4, and 5. At 16 GHz and 29.5 GHz (Figure 7(d) and Figure 7(e)), intense currents are observed along the upper part of the ground plane and the loaded stub edges, which verifies that the stub behaves as a quarter-wave parasitic resonator that contributes to higher-frequency modes and helps merge them smoothly into the existing band, as also corroborated by the parametric study in Figure 6. Thus, the current distribution plots in Figure 7 not only illustrate the radiation mechanism of the final geometry, but also justify the placement and shaping of the hexagonal aperture, patch slots, and ground stub that were systematically introduced to realize the SWB response.

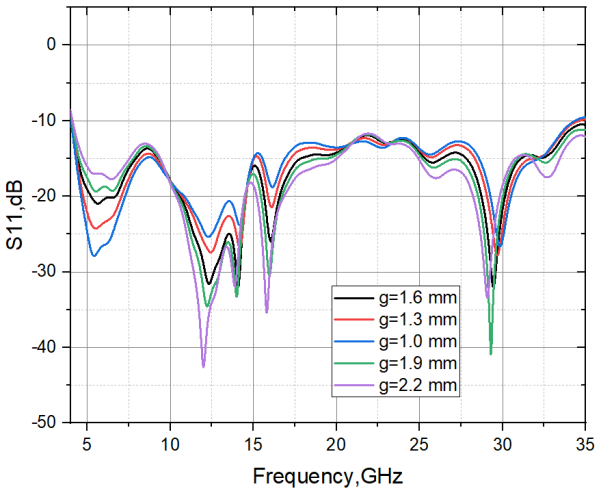

FIGURE 5. Impact of rectangular slit length on $|S_{11}|$.

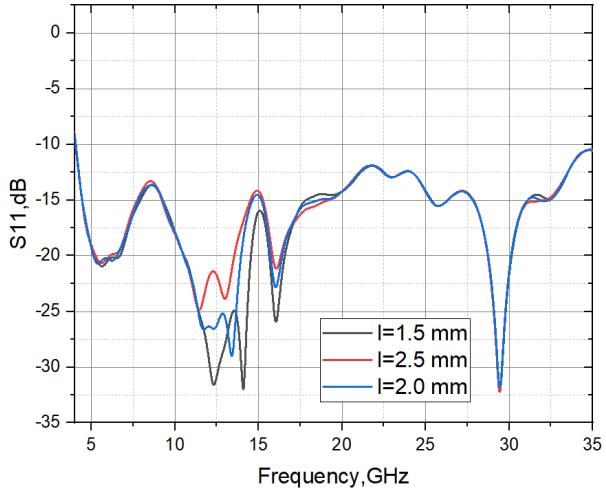

FIGURE 6. Impact of stub length on $|S_{11}|$.

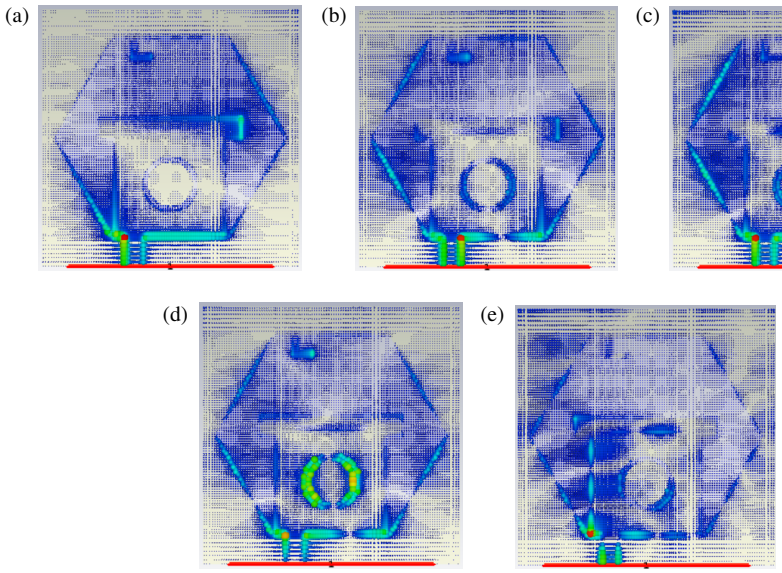

FIGURE 7. Surface current density at different frequencies: (a) 6 GHz, (b) 12.5 GHz, (c) 14 GHz, (d) 16 GHz. and (e) 29.5 GHz.

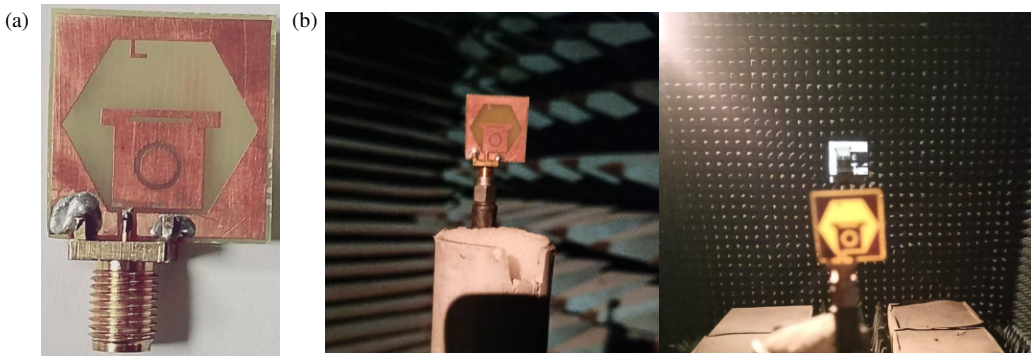

FIGURE 8. Measurement setup and antenna prototype: (a) Fabricated antenna. (b) Anechoic chamber configuration.

3. MEASURED RESULTS AND ANALYSIS

3.1. Prototype and Measurement Setup

A prototype of the antenna was fabricated on FR4, and the corresponding measurement setup is shown in Figure 8. Figure 8(a) presents the fabricated antenna, while Figure 8(b) shows the anechoic-chamber configuration used for gain and radiation-pattern measurements. In this setup, a standard gain horn is used as the transmitting antenna, and the proposed an-

TABLE 2. Performance of measured and simulated results of the proposed antenna.

Proposed Antenna-5	Substrate Thickness (mm)	IBW (GHz)	IBW ($\|S_{11}\| \leq -10$ dB)	Peak Gain (dB)	Peak Efficiency (%)
Simulated Result	1.6	4–35	158.9%	7.72	90.41
Measured Result		2–34	177.7%	6.6	82.68

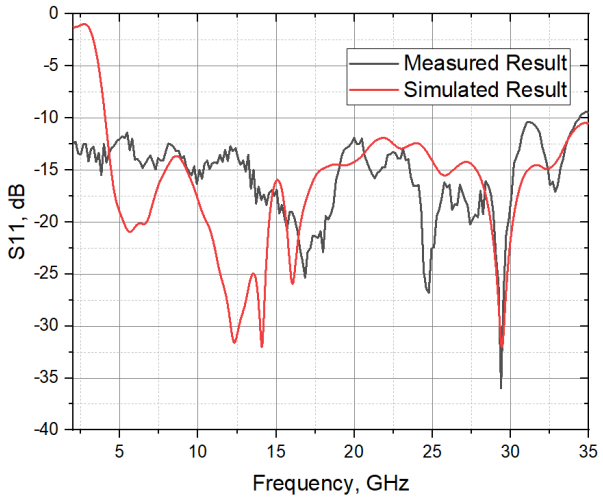

FIGURE 9. Simulated and measured $|S_{11}|$-parameters.

FIGURE 10. Antenna $|S_{11}|$ VNA measurement setup.

tenna under test (AUT) is mounted on a motorized rotary positioner. A Keysight PNA-X N5247B vector network analyzer (VNA) records the received S_{21} as the AUT is rotated over the desired angular range, and the data are calibrated against the reference horn to obtain the angular gain distribution. The antenna geometry was analyzed and optimized using CST Microwave Studio, and Figure 9 compares the simulated and measured $|S_{11}|$ responses, while Table 2 summarizes the corresponding impedance bandwidth and gain/efficiency performance. Figure 10 illustrates the VNA configuration used for the $|S_{11}|$ measurements.

3.2. Measured vs. Simulated Impedance Bandwidth ($|S_{11}|$)

Figure 9 shows that the measured and simulated $|S_{11}|$ responses agree well across the main 4–35 GHz operating region. The measured antenna achieves a -10 dB bandwidth of 2–34 GHz (177.7%), while the simulated response covers 4–35 GHz (158.9%), as summarized in Table 2. The only notable discrepancy is the appearance of an additional low-frequency resonance near 2 GHz in the measurement, which is not present in the ideal CST simulation.

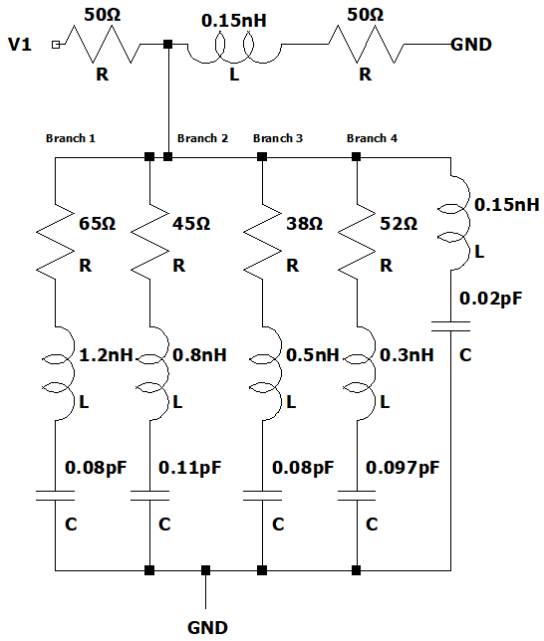

FIGURE 11. Lumped-element RLC equivalent circuit of the proposed antenna.

To better support this observation, we considered the influence of two well-known factors affecting compact CPW-fed FR4 antennas at low frequencies: (i) SMA-connector parasitic effects and (ii) variation in the effective permittivity of FR4. Including a connector model that consists of a short coaxial transition with series inductance and shunt capacitance is known to extend the electrical length of the feed region, and even modest parasitic values can introduce a resonance around 2 GHz. Similarly, FR4 substrates often exhibit ±10–15% variation in effective ε_r, especially at lower microwave frequencies; an increase in ε_r shortens the guided wavelength and can shift the structure's lowest resonance toward the 1.8–2.2 GHz region. Both mechanisms have been shown in prior CPW-fed FR4 UWB/SWB antenna studies [6, 8, 9, 19, 25, 29, 30] to generate additional low-frequency modes without affecting the intended upper wideband response.

These considerations indicate that the observed 2 GHz resonance is predominantly caused by measurement-environment and material-tolerance effects, rather than intrinsic antenna behavior. Importantly, it does not compromise the intended super-wideband operation from 4–35 GHz.

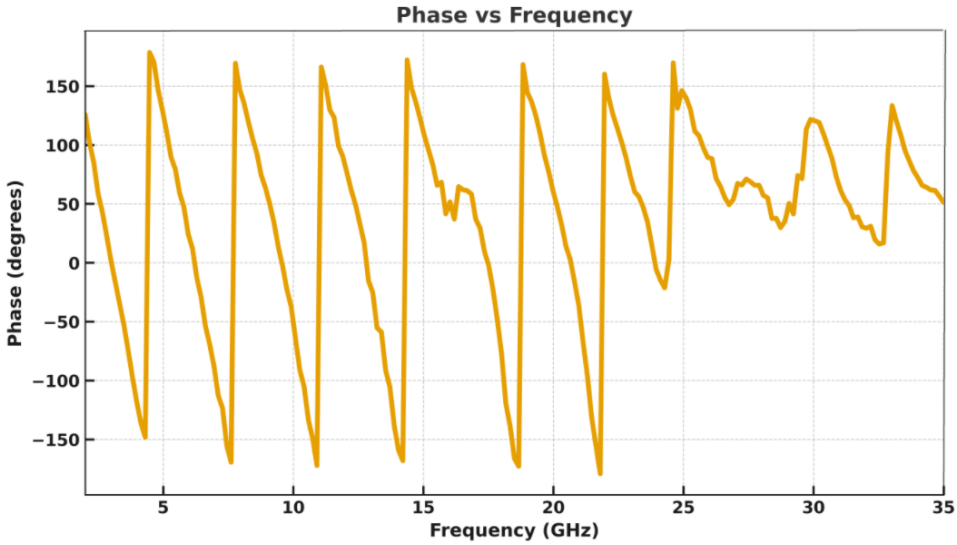

FIGURE 12. Variation of phase with frequency.

3.3. Lumped-Element Equivalent Circuit Validation

To validate the multi-resonant behavior of the proposed antenna, a lumped-element model consisting of a CPW feed inductance L_s followed by four parallel RLC branches was developed (Figure 11). The feed inductance L_s is first estimated from the CPW line geometry using standard transmission-line relations based on characteristic impedance and effective permittivity, consistent with Wheeler's strip-inductance formulation [13].

For each branch k, the inductance L_k and capacitance C_k are initially chosen so that the parallel RLC resonance satisfies (Equation (3)):

$$f_{r,k} = \frac{1}{2\pi\sqrt{L_k C_k}} \tag{3}$$

where $f_{r,k}$ corresponds to the four measured resonances at approximately 10, 17, 25, and 29.5 GHz. The relative values of L_k and C_k are guided by the dominant current paths, slot geometries, and effective electrical lengths at each mode, using classical slot-capacitance and strip-inductance relations reported in [13, 28]. As expected, higher-frequency branches exhibit lower L_k and C_k due to shorter resonant current paths, consistent with resonance-based SWB modeling approaches [31]. The resistance R_k is adjusted to match the depth and bandwidth of the corresponding measured $|S_{11}|$ dip, representing the mode's radiation and loss Q-factor.

All branch parameters are then jointly refined through impedance-curve fitting so that the modeled input impedance $Z_{\text{in}}(f)$ closely follows the measured antenna impedance around each resonance. The composite effect is evaluated by summing the admittances of the four RLC branches and the feed inductance (Equation (4)):

$$Y_{\text{in}}(j\omega) = Y_s(j\omega) + \sum_{k=1}^{4} Y_k(j\omega), \tag{4}$$

with $Z_{\text{in}}(j\omega) = \frac{1}{Y_{\text{in}}(j\omega)}$. The modeled reflection coefficient (Equation (5))

$$S_{11,\text{model}} = \frac{Z_{\text{in}}(j\omega) - 50}{Z_{\text{in}}(j\omega) + 50} \tag{5}$$

shows excellent agreement with the measured $|S_{11}|$ across 2–34 GHz, confirming that the combined contribution of the four RLC branches and the CPW feed inductance accurately represents the antenna's super-wideband behavior. This procedure aligns with established equivalent-circuit methodologies for UWB/SWB antennas as reported in [13, 28, 31].

3.4. Phase Response

The measured insertion phase plot $\angle S_{21}$ (in degrees) versus frequency across the 2–35 GHz span is shown in Figure 12. The phase exhibits a smooth, predominantly monotonic progression with the expected 360° wrapping, indicating stable dispersive behavior over the entire super-wide band. Localized steep phase turnovers coincide with resonant regions of the matching network; notably, a sharper transition is observed in the mid-20 GHz region, which is consistent with the high-Q mode later reflected as a narrow excursion in the group delay (Figure 13). Apart from these controlled roll-overs at resonance, the phase slope remains uniform, supporting the antenna's low-distortion, wideband operation and validating the multi-resonant design strategy established by the equivalent circuit in Figure 11.

3.5. Group Delay and Phase Linearity

The simulated and measured group-delay characteristics of the proposed CPW-fed SWB antenna, computed as $\tau_g = -\frac{d\phi}{d\omega}$ where ϕ is the insertion phase, exhibit excellent phase linearity throughout the 2–34 GHz operating band, as illustrated in Figure 13. The simulated group delay obtained from CST maintains values within a narrow range of approximately 0.1–0.5 ns with an average of 0.14 ns, closely matching the measured results that show a mean of 0.19 ns. Both curves confirm a nearly

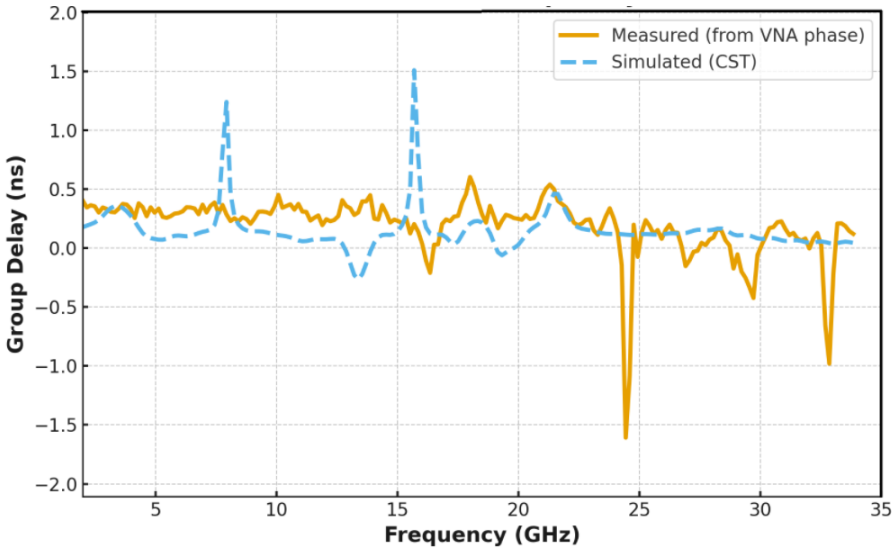

FIGURE 13. Simulated and measured group delays of the proposed antenna.

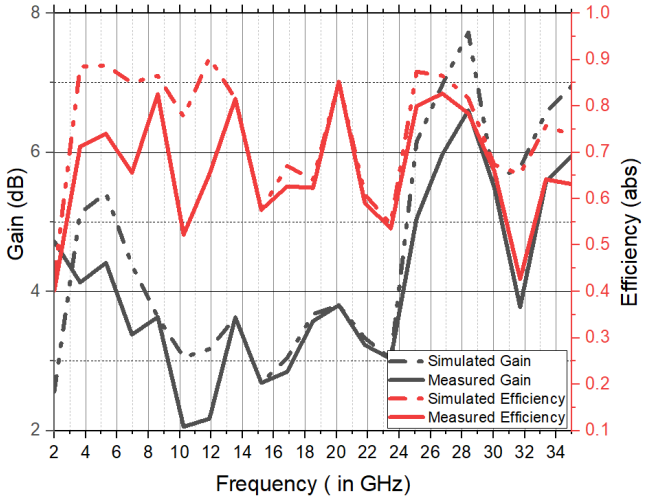

FIGURE 14. Simulated and measured gains and efficiencies of the proposed antenna.

constant τ_g, signifying low dispersion and minimal pulse distortion, which are essential for high-fidelity wideband and impulse radio UWB (IR-UWB) systems. A localized deviation about -1.61 ns near 24.4 GHz, observed in the measured response and associated with a high-Q resonant mode causing a steep phase transition, is effectively captured in the simulated trend and does not deteriorate the antenna's overall broadband dispersive performance. The strong correlation between the simulated and experimental group-delay profiles validates the proposed antenna's phase-linear behavior, confirming its suitability for ultra-wideband time-domain communication and radar applications.

3.6. Gain and Radiation Efficiency

The simulated and measured gain characteristics of the proposed antenna are presented in Figure 14, revealing consistent performance across the 2–35 GHz operational bandwidth. The antenna achieves a measured peak gain of 6.60 dB at 28.4 GHz, which compares favorably with the simulated peak gain of 7.72 dB at the same frequency. The gain progression demonstrates a distinctive pattern: lower values in the 2–15 GHz range (2.06–4.72 dB measured), moderate performance between 15–25 GHz (2.69–3.80 dB measured), and significantly enhanced gain above 25 GHz, reaching 5.05–6.60 dB measured. This gain escalation at higher frequencies correlates with improved radiation efficiency characteristics, with the antenna achieving peak simulated efficiency of 90.41% at 11.9 GHz and peak measured efficiency of 82.68% at 26.75 GHz. The efficiency performance shows strong simulated values exceeding 85% at multiple frequency points (88.75% at 5.3 GHz, 90.41% at 11.9 GHz, and 87.39% at 25.1 GHz), while maintaining reasonable efficiency throughout the operational band. The generally good agreement between simulated and measured gain characteristics, coupled with the antenna's compact $20 \times 20\,\text{mm}^2$ dimensions, enables efficient performance optimization in the millimeter-wave region, making it particularly suitable for 5G/6G applications requiring stable gain across multiple frequency bands.

3.7. Far-Field Radiation Patterns

Figures 15(a)–(e) illustrate the measured E- and H-plane co-polarisation and cross-polarisation radiation patterns of the proposed antenna at 4, 10, 17, 25, and 29.5 GHz, with each curve normalised to the measured co-polar peak at the corresponding frequency for pattern-shape assessment. At 4 GHz, the antenna exhibits a broad main-beam response with relatively low sidelobe content in the E-plane, whereas the H-plane shows a more asymmetrical profile, which is expected due to the finite ground size, CPW feed layout, and connector influence. Across 10 and 17 GHz, the radiation patterns become more directive, and the co-polar component remains dominant in the broadside region, suggesting stable linear polarisation performance over the central portion of the operating band. At 25 and 29.5 GHz, the emergence of additional lobes and minor beam tilts indicates the excitation of higher-order modes, which

TABLE 3. Comparison of the proposed antenna with other reported UWB/SWB antennas.

Ref. No.	Area (mm^2)/ Electrical size ($L \times W, \lambda_0$)	Di-electric Substrate Material (ε_r)	Operating Band (GHz)	-10 dB Impedance Bandwidth	Ratio bandwidth (RBW)	BDR (%/λ^2)	Peak Gain (dB)
[1]	21×23 ($0.21\lambda_0 \times 0.23\lambda_0$)	FR4 (4.4)	3.02–11.36	115.9%	3.76 : 1	2368	5.15
[3]	30×30 ($0.12\lambda_0 \times 0.12\lambda_0$)	FR4 (4.4)	1.21–24.66	181%	20.38 : 1	12363	9.40
[5]	88×89.9 ($0.26\lambda_0 \times 0.27\lambda_0$)	Rogers RO 3006 (6.5)	0.9–4.2	129.5%	4.67 : 1	1819	2.85
[6]	60×40 ($0.35\lambda_0 \times 0.23\lambda_0$)	Ultralam 3850 (3.14)	1.74–100	193.1%	57.47 : 1	2392	10.35
[7]	20×20 ($0.60\lambda_0 \times 0.60\lambda_0$)	FR4 (4.4)	8.95–31	108%	3.46 : 1	303	3.31
[8]	25×22 ($0.25\lambda_0 \times 0.22\lambda_0$)	FR4 (4.3)	3–11	114.2%	3.67 : 1	2076	4.10
[9]	27×25 ($0.32\lambda_0 \times 0.30\lambda_0$)	FR4 (4.4)	3.58–14	118.2%	3.91 : 1	1230	2.55
[10]	42×41 ($0.32\lambda_0 \times 0.31\lambda_0$)	Rogers RT 5880 (2.2)	2.30–11	130%	4.78 : 1	1284	2.15
[11]	46×40 ($0.31\lambda_0 \times 0.27\lambda_0$)	Rogers RT 5880 (2.2)	2.0–10.45	135.7%	5.22 : 1	1659	5.75
[12]	20×20 ($0.28\lambda_0 \times 0.28\lambda_0$)	FR4 (4.4)	4.2–25.4	143%	6.05 : 1	1824	2.70
[14]	50×50 ($0.40\lambda_0 \times 0.40\lambda_0$)	FR4 (4.4)	2.40–7.55	103.5%	3.15 : 1	647	1.85
[15]	30×30 ($0.30\lambda_0 \times 0.30\lambda_0$)	FR4 (4.4)	3.04–11	113%	3.62 : 1	1223	5.10
[16]	27×27 ($0.19\lambda_0 \times 0.19\lambda_0$)	FR4 (4.4)	2.12–14	147%	6.60 : 1	4038	6.04
[17]	17×20 ($0.21\lambda_0 \times 0.25\lambda_0$)	FR4 (4.4)	3.78–29.28	154.79%	7.75 : 1	2868	4.58
[18]	70×30 ($0.46\lambda_0 \times 0.20\lambda_0$)	Rogers RT 5880 (2.2)	1.95–4.5	80%	2.31 : 1	902	3.85
[19]	29×24 ($0.27\lambda_0 \times 0.22\lambda_0$)	FR4 (4.4)	2.80–11.50	121.6%	4.11 : 1	2006	3.65
[20]	21×9 ($0.20\lambda_0 \times 0.08\lambda_0$)	FR4 (4.4)	2.8–11.4	121.1%	4.07 : 1	7355	2.35
[21]	50×40 ($0.55\lambda_0 \times 0.44\lambda_0$)	Rogers RT 5880 (2.2)	3.28–10.4	103.86	3.17 : 1	434	7.20
[25]	20×29 ($0.21\lambda_0 \times 0.30\lambda_0$)	Rogers RT 5880 (2.2)	3.1–10.5	108%	3.39 : 1	1744	3.55
[26]	14.8×14.8 ($0.10\lambda_0 \times 0.10\lambda_0$)	FR4 (4.4)	2–16	155%	8.00 : 1	15922	13.10
[27]	23.5×35 ($0.14\lambda_0 \times 0.21\lambda - 0$)	FR4 (4.4)	1.78–30	177.5%	16.85 : 1	6130	4.45
[29]	68×33 ($0.04\lambda_0 \times 0.02\lambda_0$)	FR4 (4.4)	0.17–13.5	195%	79.41 : 1	270618	1.85
[30]	25×17 ($0.24\lambda_0 \times 0.17\lambda_0$)	FR4 (4.4)	2.94–22.2	153.22%	7.55 : 1	3754	5.18
[31]	40×30 ($0.31\lambda_0 \times 0.23\lambda_0$)	FR4 (4.4)	2.31–40.0	188.56%	17.32 : 1	2644	3.66
Proposed Antenna	20×20 ($0.13\lambda_0 \times 0.13\lambda_0$)	FR4 (4.4)	2–34	177.7%	17 : 1	9996	6.60

is typical for electrically small FR-4-based antennas operating deep into millimetre-wave frequencies. Nonetheless, in all cases, the cross-polarisation remains comparatively lower than the co-polar response within the main-beam region, demonstrating that the proposed antenna maintains practically acceptable polarisation purity across the measured SWB range. This observed behaviour aligns with the front-to-back ratio trend in Figure 16 and the peak-gain characteristics summarised in Table 2, confirming consistent broadside radiation and effective suppression of backward radiation across the entire measured band.

Figure 16 illustrates the measured front-to-back ratio (FBR) of the proposed CPW-fed super-wideband antenna, extracted from the co-polarised E- and H-plane cuts at 4, 10, 17, 25, and 29.5 GHz. The FBR is computed as the difference (in dB) between the co-polar magnitude at boresight ($\theta \approx 0°$) and that in the opposite direction ($\theta \approx 180°$), thereby quantifying the relative strength of forward and backward radiation along the main axis. The resulting curves show FBR values typically in the range of a few decibels, with near-symmetric forward/backward levels at the lower frequencies and modest forward dominance in certain cases (e.g., the H-plane at 29.5 GHz). This behaviour is consistent with the quasi-omnidirectional patterns observed in Figure 15 and confirms that the antenna is designed primarily for broad coverage rather than highly unidirectional radiation. The smooth variation of FBR with frequency, without abrupt reversals or deep nulls, supports the suitability of the proposed antenna for wideband sensing and communication scenarios where a stable overall pattern behaviour is more critical than extreme back-lobe suppression.

The proposed antenna is compared with other published ultra/super wideband antennas in Table 3. The ratio bandwidth for each antenna is calculated as f_H/f_L, where f_L and f_H are the lower and upper -10 dB impedance-band edges, and the BDR is obtained as IBW(%)$/(\lambda_L\lambda_W)$, with $\lambda_L = L/\lambda_0$ and $\lambda_W = W/\lambda_0$ denoting the electrical length and width at f_L. These RBW and BDR values are computed consistently for all referenced antennas using their reported -10 dB bands, physical dimensions, and fractional IBW. Better results are shown

(a)

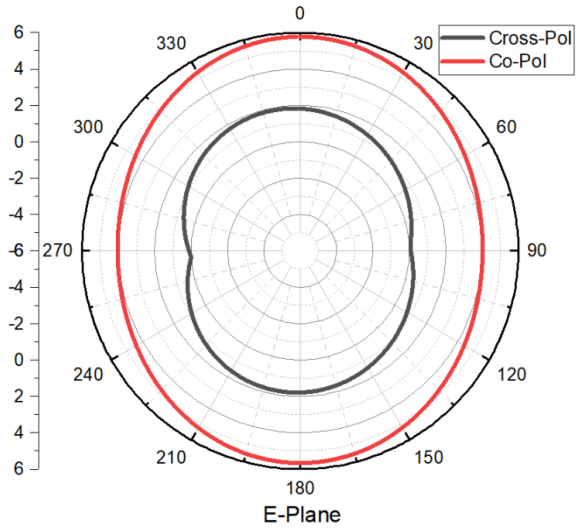
Cross-Pol
Co-Pol
E-Plane

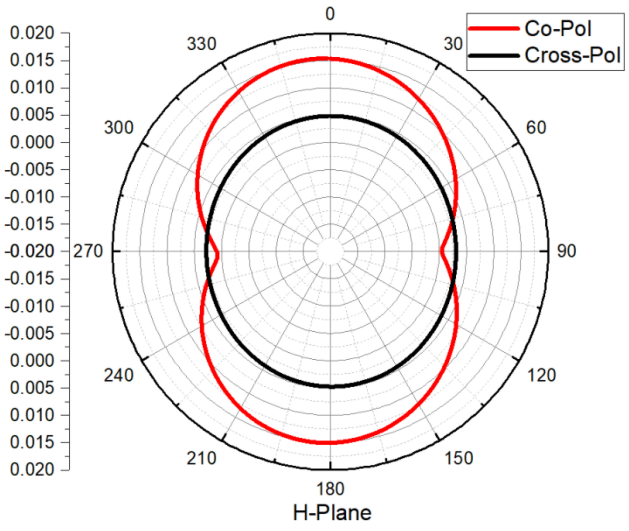
Co-Pol
Cross-Pol
H-Plane

(b)

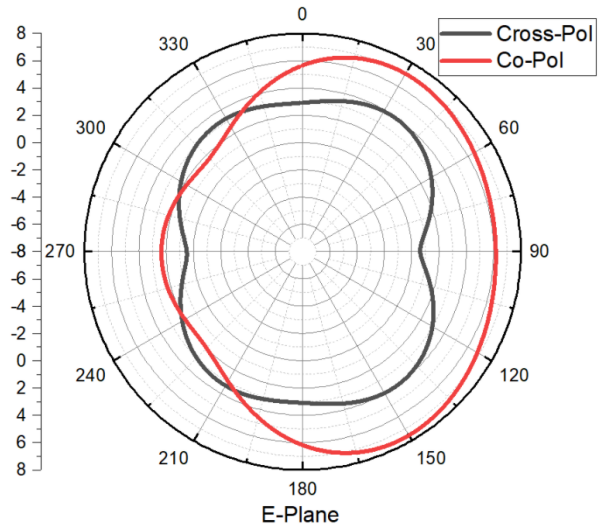
Cross-Pol
Co-Pol
E-Plane

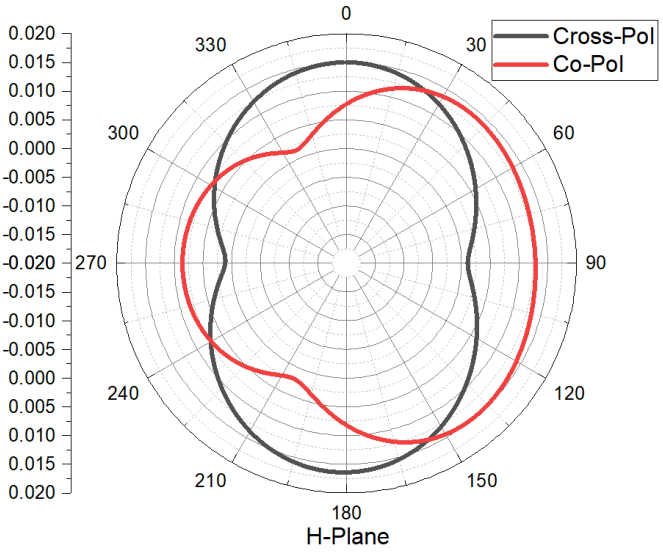
Cross-Pol
Co-Pol
H-Plane

(c)

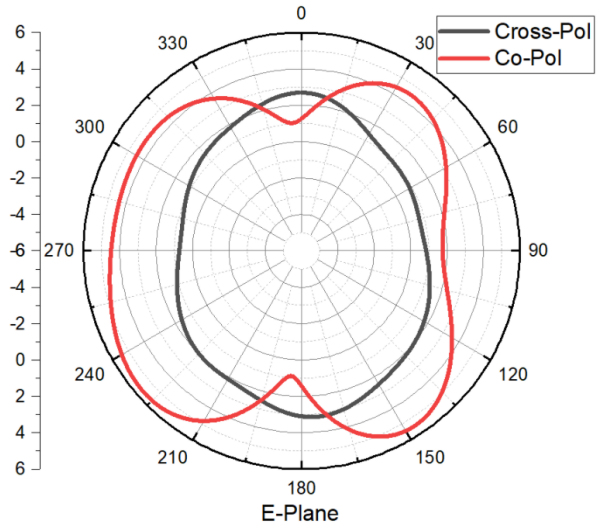
Cross-Pol
Co-Pol
E-Plane

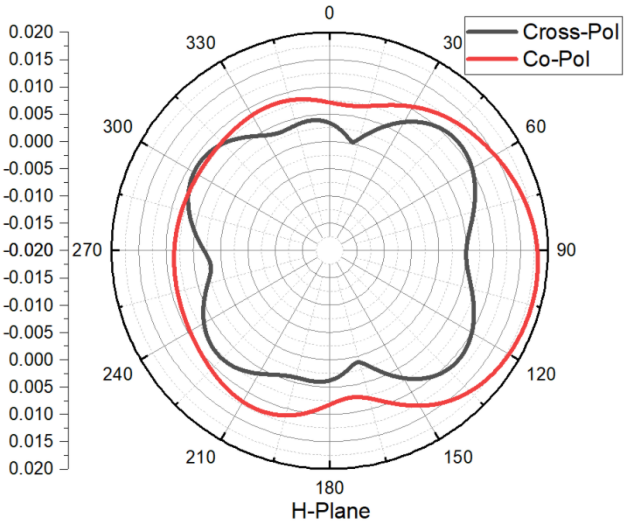
Cross-Pol
Co-Pol
H-Plane

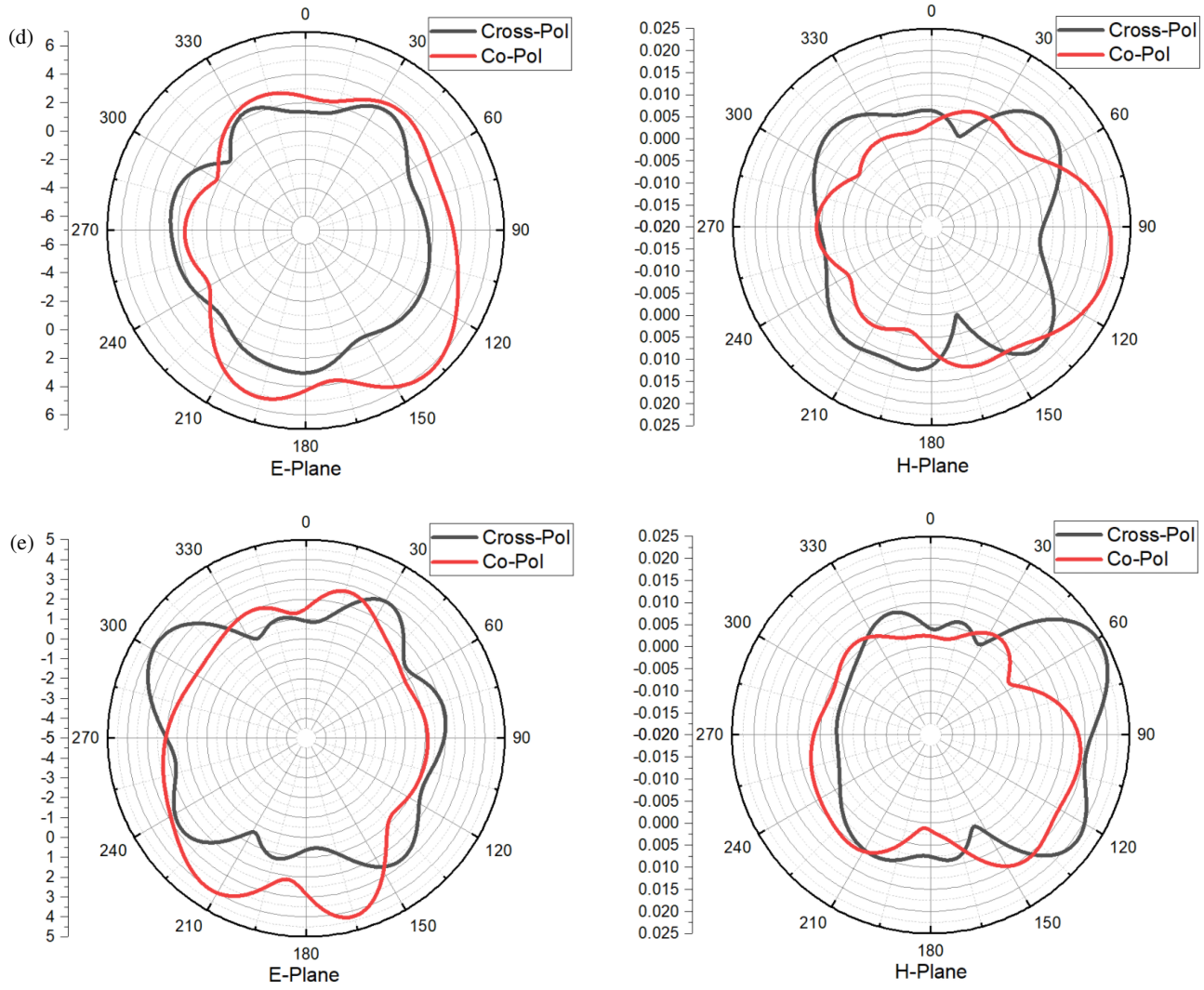

FIGURE 15. Radiation patterns (E- and H-plane). (a) 4 GHz, (b) 10 GHz, (c) 17 GHz, (d) 25 GHz, and (e) 29.5 GHz.

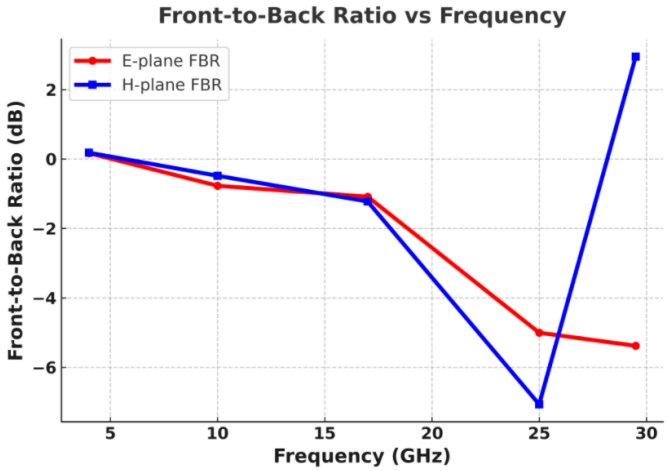

FIGURE 16. Measured FBR of the proposed CPW-fed antenna.

by the proposed antenna in terms of antenna profile, IBW, and gain.

4. CONCLUSION

A small, SWB CPW-fed antenna is introduced for use in different wireless and sensing applications. The full design is incorporated into a hexagonal cut in the antenna ground to make the suggested antenna small and space-efficient, while its 2–34 GHz operating band enables coverage of sub-6 GHz 5G, WLAN/WiMAX, C/X/Ku/Ka radar and imaging bands, and millimeter-wave 5G/early 6G links within a single compact radiator. Excellent super-wideband performance of 177.7 percent (2 GHz–34 GHz) is demonstrated by the measured result. The apparatus maintains a consistent omnidirectional radiation pattern and shows a measured peak gain of 6.60 dB. The antenna has been prototyped on 1.6 mm thick FR4 substrate material and consists of a slotted patch and hexagonal ground plane. At its lowest operating frequency of 2 GHz, the antenna measures $20 \times 20\,\text{mm}^2$. The proposed antenna can operate in the 2 GHz to 34 GHz range owing to the slotted patch's efficient coupling with the hexagonal slot in the ground plane.

REFERENCES

[1] Awan, D., S. Bashir, S. Khan, S. S. Al-Bawri, and M. Dalarsson, "UWB antenna with enhanced directivity for applications in microwave medical imaging," *Sensors*, Vol. 24, No. 4, 1315, 2024.

[2] Jalilvand, M., X. Li, L. Zwirello, and T. Zwick, "Ultra wideband compact near-field imaging system for breast cancer detection," *IET Microwaves, Antennas & Propagation*, Vol. 9, No. 10, 1009–1014, 2015.

[3] Sekhar, M. and N. Suman, "CPW fed super-wideband antenna for microwave imaging application," *Progress In Electromagnetics Research C*, Vol. 130, 201–212, 2023.

[4] AlSawaftah, N., S. El-Abed, S. Dhou, and A. Zakaria, "Microwave imaging for early breast cancer detection: Current state, challenges, and future directions," *Journal of Imaging*, Vol. 8, No. 5, 123, 2022.

[5] Gharaati, A., M. S. Ghaffarian, H. Saghlatoon, M. Behdani, and R. Mirzavand, "A low-profile wideband circularly polarized CPW slot antenna," *AEU — International Journal of Electronics and Communications*, Vol. 129, 153534, 2021.

[6] Dey, S., M. S. Arefin, and N. C. Karmakar, "Design and experimental analysis of a novel compact and flexible super wide band antenna for 5G," *IEEE Access*, Vol. 9, 46 698–46 708, 2021.

[7] Dhara, R., "Quad-band circularly polarized CPW-fed G-shaped printed antenna with square slot," *Radioelectronics and Communications Systems*, Vol. 63, No. 7, 376–385, 2020.

[8] Ahmad, S., U. Ijaz, S. Naseer, A. Ghaffar, M. A. Qasim, F. Abrar, N. O. Parchin, C. H. See, and R. Abd-Alhameed, "A jug-shaped CPW-fed ultra-wideband printed monopole antenna for wireless communications networks," *Applied Sciences*, Vol. 12, No. 2, 821, 2022.

[9] Jameel, M. S., Y. S. Mezaal, and D. C. Atilla, "Miniaturized coplanar waveguide-fed UWB antenna for wireless applications," *Symmetry*, Vol. 15, No. 3, 633, 2023.

[10] Hossain, A., M. T. Islam, M. T. Islam, M. E. H. Chowdhury, H. Rmili, and M. Samsuzzaman, "A planar ultrawideband patch antenna array for microwave breast tumor detection," *Materials*, Vol. 13, No. 21, 4918, 2020.

[11] Islam, M. T., M. T. Islam, M. Samsuzzaman, H. Arshad, and H. Rmili, "Metamaterial loaded nine high gain vivaldi antennas array for microwave breast imaging application," *IEEE Access*, Vol. 8, 227 678–227 689, 2020.

[12] Dhara, R., "Design of a miniaturized CPW fed Z-shaped monopole antenna using theory of characteristics modes for bandwidth enhancement," *Sādhanā*, Vol. 46, No. 2, 87, 2021.

[13] Wheeler, H. A., "Transmission-line properties of parallel strips separated by a dielectric sheet," *IEEE Transactions on Microwave Theory and Techniques*, Vol. 13, No. 2, 172–185, 1965.

[14] Fu, Q., Q. Feng, and H. Chen, "Design and optimization of CPW-fed broadband circularly polarized antenna for multiple communication systems," *Progress In Electromagnetics Research Letters*, Vol. 99, 65–74, 2021.

[15] Elhabchi, M., M. N. Srifi, and R. Touahni, "A novel modified u-shaped microstrip antenna for super wide band (SWB) applications," *Analog Integrated Circuits and Signal Processing*, Vol. 102, No. 3, 571–578, 2020.

[16] Kaur, K., A. Kumar, and N. Sharma, "A novel design of ultra-wideband CPW-fed printed monopole antenna for Wi-MAX, WLAN and X-band rejection characteristics," *Analog Integrated Circuits and Signal Processing*, Vol. 114, No. 1, 143–157, 2023.

[17] Mali, R., D. Lodhi, and S. Singhal, "Quad broadband circularly polarized CPW FED cleaver shaped extended UWB MIMO antenna for 5G, C, K and millimeter wave applications," *Analog Integrated Circuits and Signal Processing*, Vol. 118, No. 2, 271–290, 2024.

[18] Islam, M. S., M. T. Islam, and A. F. Almutairi, "A portable non-invasive microwave based head imaging system using compact metamaterial loaded 3D unidirectional antenna for stroke detection," *Scientific Reports*, Vol. 12, No. 1, 8895, 2022.

[19] Hossain, A., M. T. Islam, A. F. Almutairi, M. S. J. Singh, K. Mat, and M. Samsuzzaman, "An octagonal ring-shaped parasitic resonator based compact ultrawideband antenna for microwave imaging applications," *Sensors*, Vol. 20, No. 5, 1354, 2020.

[20] Srivastava, G., A. Mohan, and A. Chakrabarty, "Compact reconfigurable UWB slot antenna for cognitive radio applications," *IEEE Antennas and Wireless Propagation Letters*, Vol. 16, 1139–1142, 2016.

[21] Yadav, S. K., A. Kaur, and R. Khanna, "Cylindrical air spaced high gain dielectric resonator antenna for ultra-wideband applications," *Sādhanā*, Vol. 45, No. 1, 163, 2020.

[22] Deshmukh, A. A. and K. P. Ray, "Analysis and design of broadband U-slot cut rectangular microstrip antennas," *Sādhanā*, Vol. 42, No. 10, 1671–1684, 2017.

[23] Deshmukh, A. A., D. Singh, and K. P. Ray, "Modified designs of broadband E-shape microstrip antennas," *Sādhanā*, Vol. 44, No. 3, 64, 2019.

[24] Kwe, N. B., V. Yadav, M. Kumar, S. V. Savilov, M. Z. A. Yahya, and S. K. Singh, "A comparative study of dielectric substrate materials effects on the performance of microstrip patch antenna for 5G/6G application," *Journal of Materials Science: Materials in Electronics*, Vol. 35, No. 24, 1617, 2024.

[25] Zhang, S., Y. Zhong, Y. Zhou, Y. Guo, and C. Ji, "Design of a symmetric open slot antenna for UWB applications," *IEICE Electronics Express*, Vol. 16, No. 20, 20190533, 2019.

[26] Negi, D. and R. Khanna, "A high gain CPW fed metamaterial antenna for UWB applications," *Progress In Electromagnetics Research C*, Vol. 132, 51–63, 2023.

[27] Chaudhary, A. K. and M. Manohar, "A modified swb hexagonal fractal spatial diversity antenna with high isolation using meander line approach," *IEEE Access*, Vol. 10, 10 238–10 250, 2022.

[28] Balanis, C. A., *Antenna Theory: Analysis and Design*, John Wiley & Sons, 2016.

[29] Kumar, S., K. W. Kim, H. C. Choi, S. Saxena, R. Tiwari, M. K. Khandelwal, S. K. Palaniswamy, and B. K. Kanaujia, "A low profile circularly polarized UWB antenna with integrated GSM band for wireless communication," *AEU — International Journal of Electronics and Communications*, Vol. 93, 224–232, 2018.

[30] Tiwari, R. N., P. Singh, and B. K. Kanaujia, "A modified microstrip line fed compact UWB antenna for WiMAX/ISM/WLAN and wireless communications," *AEU — International Journal of Electronics and Communications*, Vol. 104, 58–65, 2019.

[31] Sharma, V., Gunaram, J. K. Deegwal, and D. Mathur, "Super-wideband compact offset elliptical ring patch antenna for 5G applications," *Wireless Personal Communications*, Vol. 122, No. 2, 1655–1670, 2022.